ANALYSIS OF OCEAN HORIZON IMAGE MEASUREMENTS IN THE MWIR

by

E.H. Takken, J.T. Caulfield, E.J. Stone, E. P. Shettle, and R.G. Priest
Naval Research Laboratory, Washington DC 20375-5338

M.D. Mermelstein
Maryland Advanced Development Laboratory, Greenbelt MD 20770

R. York
SFA, Inc., Landover MD 20785

To Appear in the Proceedings of
the IRIS Specialty Group Meeting on
Targets, Backgrounds, and Discrimination

San Antonio, TX
26-28 January 1993

ANALYSIS OF OCEAN HORIZON IMAGE MEASUREMENTS IN THE MWIR

January 1993

E.H. Takken, J.T. Caulfield, E.J. Stone, E. P. Shettle, and R.G. Priest
Naval Research Laboratory, Washington DC 20375-5338

M.D. Mermelstein
Maryland Advanced Development Laboratory, Greenbelt MD 20770

R. York
SFA, Inc., Landover MD 20785

ABSTRACT

During November 1992 NRL participated in an IRAMMP field test using a new staring midwave IR sensor in an open ocean environment. The thrust of the measurements was the characterization of clutter just above and below the horizon. This paper reports on the performance of the NRL sensor and the image data taken with it, and summarizes the recordings made of the horizon radiance profile, solar glint, night sea and sky radiance, the Gulf Stream temperature transition, and cloud structure. A previously reported radiance model, based on surface wave slope statistics, has been refined and agrees well with measurements of both surface emissivity and solar sea glint.

INTRODUCTION

On November 8-15 1992 Navy personnel conducted a joint exercise to obtain calibrated infrared image data in an open ocean environment. The test was performed at Diamond Shoals Light Tower, an 80-foot Coast Guard tower 12 miles offshore near Cape Hatteras, North Carolina. This location is within a few kilometers of an eddy of the Gulf Stream, which is 6-8C warmer than the coastal water, and often warmer than the local air mass. NRL field tested a new midwave IR staring sensor; the resulting data are reported in this paper. NSWC White Oak Laboratory operated the IRAMMP dual-band (midwave and longwave) IR scanning sensor, and MIT Lincoln Labs operated a PtSi-based staring midwave IR imager. Their results will be reported separately. Meteorological data of the atmosphere and sea were collected simultaneously from the NCCOSC instrumented aircraft, from a buoy, a surface boat, and from sensors on the lighthouse. Areté Associates and QuesTech, Inc. provided planning, logistical support, environmental measurements, and archiving of the data.[1] Weather conditions were partly cloudy throughout, with varying sea states. Calibrated sun glint and moon glint near-horizon data were obtained, as well as imagery of the Gulf Stream temperature change, clouds near and above the horizon, cloud shadows on the sea, and the horizon under various conditions.

SENSOR

The sensor used by NRL in the Diamond Shoals Light test consisted of a 256 x 256 InSb IR focal plane array from Amber Engineering mated to an f/2.3, 300 mm refracting telescope. The data reported here were all taken with the internal broad-band cold filter. An NRL order for Amber's versatile electronics was in place, but the equipment actually used during the field test was more limited, so that calibration for non-uniformity correction was time consuming and only a limited amount of data could be recorded. Recorded radiometric calibrations in some cases lacked an additive constant; these cases will be referred to here as "relative" radiance units. Laboratory tests of similar arrays have shown[2] noticeable drift over periods of less than two hours, and the equipment in the field exhibited spatial noise degradation after 40 min. Daily air temperature on the tower ranged from near freezing to 20C, so that wind cooling and solar heating of the optics was a concern. Nonuniformity corrections needed to be performed frequently. Significant parameters of the array and sensor are:

Array:

- 256 x 256 staring InSb
- detector pitch: 38 μm; active extent: 34 μm.
- quantum efficiency: 0.4
- D star: 3×10^{11} cm-$\sqrt{Hz}$/w at f/2.3, 16 msec integration time and background flux 10^{14} ph/cm^2/sec
- charge capacity: 10^6 carriers

Sensor:

- IFOV: 0.127 milliradian
- TFOV $1.86^\circ \times 1.86^\circ$
- NEI temporal: 1.3×10^{-15} W/cm^2
- NEI spatial: 3.3×10^{-14} W/cm^2
- Waveband 3.1 - 4.9 μm.
- Focal length: 300 mm
  aperture: 130 mm

DATA SET

The IR data taken by NRL consists of approximately 60 nonuniformity-corrected images gathered over a period of 3 days in variably cloudy conditions with wind speeds from near calm to 20 knots, and significant wave heights from 1 to 2 meters, peak-to-trough. Absolute radiometric calibration was achieved with 29 of these scenes, and calibration to within an additive constant with 30 scenes. For two other qualitative images the calibration is known only approximately. Imagery obtained included:

- Horizon imagery at sunrise with clouds above horizon
- The change in sea surface temperature at the edge of the Gulf Stream
- The horizon under a variety of conditions both distinct and indistinct
- Sun glint on water, with cloud shadows; solar elevation ~ 36°
- Backlit cloud structure at line-of-sight elevations of 0-30°
- Sky with minimal cloud content at different elevations
- Night water scene, with moon near full
- Night clouds illuminated by warm water below
- The clear night sky as a function of elevation
- Water waves at azimuths away from sun with wave heights ~ 2 m

- Targets of opportunity, including the met aircraft, a sailboat and large tanker ship.

Ancillary imagery was also gathered, in the form of a video cassette recording of the IR, and .lh 9 visible-light still photographs.

OCEAN SURFACE RADIANCE

Models of observed ocean radiance have been constructed by several authors[3-6]. A new statistical model for the measured radiance is presented in the Appendix. The ocean surface, within the sensor field-of-view, is divided into surface elements (facets) whose characteristic dimension is determined by the wave slope coherence length. The facet orientation is described by a normal distribution which is a function of the look direction wave slope and the orthogonal wave slope. A wave slope power spectral density function, obtained from the radar community, is utilized to obtain the two orthogonal wave slope variances for the normal distribution. This power spectral density is a function of the wind speed, wind direction, and water temperature. The population of observable facets is limited to those having positive slopes along the look direction, thereby yielding a non-zero mean slope. The reflectivity of the surface element is determined from the Fresnel equations for reflection from the air/water interface. Associated with a surface element are four sources of infrared radiation: (i) blackbody emission, (ii) reflected sky radiance, (iii) solar glint, and (iv) reflected scattered sunlight. In addition to these sources of radiation is the thermal emission of the atmosphere along the path from the sensor to the ocean surface element. The determination of these infrared radiation sources as a function of wave slope, along with the wave slope probability density function, permits the computation of the mean radiance and the radiance variance. An estimation of the number of surface elements in conjunction with the central limit theorem allows the computation of the radiance standard error or clutter.

APPLICATION TO PHENOMENOLOGY

Sky Radiance Gradient and Horizon Feature: Fig. 1 shows the NCCOSC aircraft inbound at a range of about 4 km. The time was about an hour before sunset with the sun well to the right so that the water wave structure is due to differences in surface emissivity and sky reflection rather than to solar glint or whitecaps. The graph gives row-average radiance in a vertical scan through the scene. The vertical radiance gradient in the sky is 0.010-0.011 $W/m^2/sr$ per degree of elevation. The air is cooler than the water, causing an upward rise in radiance at the horizon. This rise would become an abrupt step in good seeing conditions.[5] Negative values of the air-sea temperature difference (ASTD), meaning that the air is colder than the water, are also significant because they cause light rays to bend upward, producing a mirage effect.

Fig. 2 shows a night scene of the horizon above the Gulf Stream to the east of the tower. Visibility is poorer than in Fig. 1, and the horizon profile step is somewhat smoothed and, were it not for the Gulf Stream, would be negative. The moon is near full at 40° elevation above the line of sight. Although to the eye the sea was covered in moon glint, the "glint" apparent in the IR imagery is due entirely to variation in water emissivity and sky reflection with varying wave surface angle. In the midwave IR the moon's contribution to observed radiance is negligible (5 orders of

magnitude less than the sun). This became clear to the experimenters when a change in azimuth of the sensor view produced no change in the IR appearance of the sea. The speckle in the surface radiance of Fig. 2 is due largely to the effect of wave-slope variability on water emissivity. The reflected cold sky radiance contribution is expected to be small.

Fig. 3 shows the ocean and sky on a different night. The speckle phenomenon in Fig. 3(a) is similar to that in Fig. 2. In Fig. 3(b) clouds in a cold sky exhibit warm bottoms in the infrared. This is due both to reflection of the warmer water below and thermal structure in the clouds.

Horizon Geometry: Viewing paths to scene locations near the horizon intercept both the water surface and bottoms of any clouds at near-tangent grazing angles. Image pixels on the sea near the horizon cover large extents of surface and so are spatially averaged, and therefore exhibit less structure than nearer sections of the water scene. Above the horizon, cloud fronts become obscured and cloud bottoms become merged so that their clutter structure is also reduced.

One aspect of this near-tangent geometry is that the horizon may exhibit solar illumination even when there is significant cloud shadowing in the foreground. Figs. 4a and 4b are examples of such horizon glint. The view is to the south at noon with the winter sun directly above the line of sight at an elevation of 30°, so that without clouds there would be glint across the entire water surface. The footprint of a 127 μradian horizon pixel here is about 2 m wide, but several kilometers long, so that intensity averaging from many solar glint wave facets must occur within these pixels.

Horizon Turbulence vs. Maximum Wave Height. Fig. 5 is a visible photograph of a passing tanker ship when it is just past the horizon. Strong horizon waviness shows up clearly against the ship background and is probably due in large part to turbulence. The mirage bow line, however, is straight right down to the water surface, indicating that strong turbulence is limited to only very low paths, the ones that pass closest to the water surface.

Another candidate for the cause of horizon waviness is the statistics of surface waves. Within a kilometers-long pixel on the tangent horizon the highest wave sticks up above the others by 20-30% of the mean wave height.[7] The raised region of water just above a non-blurred bright single pixel in Fig. 4b would appear to be such an event. This amount of height protrusion seems large, but at the horizon 15 km away the protrusion of the tallest wave becomes an angular difference of less than 100 μradian, which is less than the sensor IFOV. This means that turbulence, though much reduced on elevated paths, may be the main source of horizon line waviness.

When the air is colder than the water and thus when mirage conditions exist, the first viewing of a distant point object at maximum range will be along paths elevated from the water surface and suffering far less turbulence than those that define the horizon itself. In Fig. 4 this maximum-range view angle corresponds to the juncture of the true and mirage images. Ray bending calculations indicate that this maximum-range elevation angle is fairly independent of air-sea temperature difference, approximately 250 μradian below the geometric straight-line horizon, so long as the air is more than 0.5C colder than the water.

Low-Horizon Cloud Clutter: Low-elevation clouds can be particularly bright when they are

back-lit near sunrise or sunset. But, because of the near-tangent path incidence in the first few milliradians, structure of cloud bottoms is well averaged and weak, and one is very unlikely to see either cloud fronts or the holes through which sunlight reaches the ocean surface.

An example of low-elevation cloud structure is given in Fig.6. The scene shows dense, low-contrast stratus clouds over the warm Gulf Stream east of Diamond Shoals. Though obscured, the rising sun illuminates from behind an approximately 2 mrad high slit under the clouds just above the horizon. This structure is apparently brighter than usual for such a low position; several minutes later when the sun had risen higher the structure in this slit had virtually disappeared. In the region of uniform overcast, a calculation of the rms local variation yields a pixel pattern noise NEI of 3.3×10^{-15} W/cm^2. For a point target the effective NEI would be somewhat larger, due to signal sharing among detectors.

In the 2 mrad slit region just above the horizon the local rms spatial variation was extracted from sub-regions of the data oriented in both the azimuthal and elevation direction. The vertical structure is clearly more pronounced, apparently because of the viewing geometry, and in this direction the standard deviation of spatial scene structure was about twice that of the sensor spatial nonuniformities. But more relevant for processing in scanning sensors is the azimuthal structure. Along horizontal rows varying in length from 25 to 160 pixels, or 3 to 20 mrad in length, the measured spatial noise in this back-illuminated slit was 4.5×10^{-15} W/cm^2. The clutter level of the natural scene, without the sensor's pattern noise contribution, is thus about 3.0×10^{-15} W/cm^2.

It is important to determine the strength of clutter at angular sizes that are a small fraction of a milliradian, the relevant size of residual clutter that will pass through the spatial filter and hence limit performance of an advanced, high-resolution, point-source-detection device. There presumably is such fine-grained structure in the natural scenes, though below the spatial noise of the present sensors reported here, so the power spectral densities can not be measured to high frequencies. In lieu of an actual measurement one can do a rough extrapolation. Normal power spectral densities of cloud clutter often have $(1/f)^n$ power law dependencies with n close to 2 or larger for a one-dimensional spatial frequency and close to 3 or larger for a two-dimensional spatial frequency. This implies a clutter intensity dropping off approximately linearly with angular size or possibly faster with a 1.5 or more exponential dependence. If this holds in spite of the tangent geometry low over the horizon, clutter strength at 0.2 mrad will be some 10 to 15 times lower than that at 2 mrad or on a scale somewhat below 10^{-15} W/cm^2.

Emissivity of Surface with Wave Slopes: The Gulf Stream near Diamond Shoals and the availability of the NCCOSC meteorology aircraft provided a means of measuring the emissivity of the wave-slope-dominated ocean surface just below the horizon. Fig. 7 shows a sunrise scene on a day with good visibility when the Gulf Stream was particularly distinct. The morning clouds are again quite dense over the warm water, and at the time of the image the sun had risen just far enough to begin illuminating the tops of these clouds. The plot accompanying this scene graphs row average radiance, up to an additive unknown constant. The radiance data exhibits a step in radiance across the Gulf Stream boundary, which extends for ~250 m, of 0.020 W/m^2/sr.

The NCCOSC meteorology aircraft flew an outward path along the line of sight and used a

downward looking radiometer to measure surface temperature at points separated by ~450 m. The surface temperature in the Gulf Stream was 25.2C; in the adjacent sea closer to the sensor the temperature was 18.5C, a change of 6.7C. From meteorology data and a LOWTRAN[8] calculation it is estimated that transmission along the 4.85 km path to the the Gulf Stream boundary at 3.75 mrad dip angle was 0.37. The radiance step was calculated using the model and found to be 0.028 $W/m^2/sr$. This calculated step exceeds the observation by a factor of 1.4.

Solar Glint: Fig. 8 shows an image of sun glint on the ocean broken by two cloud shadows. The line of sight is along the solar azimuth; the solar elevation is 36°. The graph shows row averages of radiance. Since the contributions to apparent radiance of water thermal emission, sky reflection, atmospheric path radiance and transmission will be approximately the same for the illuminated and shadowed areas, the radiance difference between these areas, 0.7 $W/cm^2/sr$, is a good estimate of the solar glint contribution. The glint contribution calculated from the present model is 2.6 $W/m^2/sr$, which when multiplied by the calculated transmittance becomes 0.96 $W/m^2/sr$ at the sensor. Again, this is a factor of 1.4 higher than the measurement, which may indicate either a systematic error in the sensor calibration or a need for refinement of the model.

Fig. 9 shows MWIR results from an experiment performed in the Florida Keys in July 1990[9] using the dual-band IRAMMP sensor. This is the measured radiance profile including solar glint in a 3.89 to 4.06 μm bandwidth as a function of angle above the horizon. The sun was present at an elevation angle of 36 degrees above the sensor line of sight and one degree to the side in azimuth. The wind speed was 4 m/s.

The modeling of this case includes all possible sources of radiation as a function of elevation angle. There are two contributions to the radiance above the horizon - the sky radiance and the scattered sunlight. These contributions were determined from the LOWTRAN 7 code, fit to parametrized trial functions and combined as a single sky radiance contribution. The MWIR ocean surface radiance is dominated by solar glint which generates a radiance step as the horizon is crossed. Also contributing to the radiance below the horizon are the reflected sky radiance including scattered sunlight, thermal emission from the water, and path radiance. These four calculated radiance contributions for below the horizon are plotted in Fig. 10.

The reflected sky radiance, L_{sky}, decreases slowly with look-down angle because of two factors. At deeper look-down angles the surface reflectivity is reduced and the sensor's view is directed upward to cooler regions of the sky. Conversely, the thermal radiance of the water surface, L_w, increases with look-down angle. The atmospheric path radiance, L_p is greatest on the long path to the horizon. These three lesser contributors to the surface radiance each contribute between 0.01 and 0.1 $W/m^2/sr$. The strength of major mid-wave contributor, the solar glint, L_g, starts at approximately 1.3 $W/m^2/sr$ at the horizon and increases with lowered view angle. At the horizon solar reflection is less probable because it is from facet angles in the tail of the wave-slope distribution, but at steeper look-down view angles these reflections occur at specular angles closer to the mean of the wave-slope distribution. There is also clutter averaging of the many glint sources at the horizon in the long-footprint pixels there.

The total calculated radiance as a function angle above the horizon is shown in Fig. 9 as

filled squares. The standard error deviation also computed in the Appendix from Eq. (21) is shown as the error bars and represents the rms clutter generated by the solar glint reflected by the sea surface. There is good agreement between the calculated and measured values of both total and rms radiance.

Longwave IR (8 - 12 μm) images were also recorded in the Key90 field test, although not analyzed in detail here. It is possible nonetheless to make a general statement about the extension of this analysis to those wavelengths. The solar component is lower in the longwave than in the midwave by a factor of 30 to 50. In the longwave, sunglint will be a minor component of the total radiance, and wave-angle modulated surface speckle will thus have the same characteristics as midwave night or solar-free daytime images.

CONCLUSIONS

- A set of midwave infrared image data of high quality of near-horizon phenomena in an open ocean environment has been measured using a staring IRFPA sensor.
- A computational model for the IR radiance and clutter of the ocean surface has been developed, has produced good quantitative results, and will continue to be refined.
- The sea surface wave structure produces a corresponding spatial radiance structure of some intensity in nearly all conditions, due to the wave-slope dependence of the emissivity and reflectance, regardless of the presence of discrete sources such as the sun.
- There is a strong potential for sun glint at the horizon even in mostly cloudy conditions.
- Horizon geometry creates a very long pixel footprint on the water or on any cloud base so that 1) clutter structure either on the water on low clouds is reduced, 2) the likelihood of cloud shadowing of the horizon is low, and 3) the number of wave swells within the horizon pixel is large and the highest protudes significantly above the rest.
- Horizon line waviness can be on the order of 1/8 mrad. Turbulence and the maximum wave height effect are apparently both involved.
- Background clutter intensity ranged from 1-2 times the sensor noise to over half the dynamic range during the field test, indicating that current research sensors are sufficient for IRST applications.
- Examples of low-elevation cloud structure measured were: 6.5×10^{-15} W/cm^2 in a 2 mRad square region at the horizon; 3×10^{-15} W/cm^2 across 30-160 mRad scan at the horizon both in a back-lit slit at sunrise under an otherwise dense cloud; and 1 to 2×10^{-14} W/cm^2 in a 3-4 mRad square at 10-15 mRad elevation, all during conditions of significant ray upbending.
- Maximum range of detection: When the air is colder than the water ranges are shortened by ray upbending. Then the initial elevation angle at which a distant point source can first be seen is above, not at the apparent horizon, and is always close to 1/4 mrad below the geometric straight-line tangent to the earth circumference. This is the same elevation angle as the merge point of mirage and normal images of extended sources. Turbulence is far less along paths to this position than it is along paths skimming the horizon.

REFERENCES

1. Requests for this IRAMMP data should be addressed to M. Eggleston, QuesTech, Inc., fax 703-760-1061.

2. K.A. Sarkady, J.T. Caulfield, D.A. Scribner, M.R. Kruer, and M. Johnson, "Performance and Stability Measurements on Several Large Area Staring IRFPA's," Proceedings of the 1992 Meeting of the IRIS Specialty Group Meeting on Infrared Detectors.

3. R.G. Priest and I.B. Schwartz, "A Probabilistic Model of the Apparent Radiance of a Rough Sea," Naval Research Laboratory Memorandum Report 6092, March 1988.

4. D. Fraedrich, "Spatial and Temporal Infrared Radiance Distributions in Solar Sea Glint," Ocean Optics IX, M.A. Blizard, Ed., Proceedings SPIE Vol. 925, p. 392-397 (1988)

5. R.G. Priest, E.P. Shettle, and E.H. Takken, "High Resolution Imagery of the Sea Horizon: Data and Modeling," Proceedings of the IRIS Specialty Group on Targets, Backgrounds, and Discrimination, January 1992, ERIM document 213400-128-X(I).

6. P. Davis, A. Daniell, M. Farber, and S. Hemple, "Infrared Ocean Clutter at Low Grazing Angles: Data Analysis Results and 1-D Simulation," Proceedings of the IRIS Specialty Group on Targets, Backgrounds, and Discrimination, January 1992, ERIM document 213400-128-X(I).

7. R. G. Priest, *et al.*, 1992, *op.cit.* When 1000 to 10000 values are generated at random in accordance with a Gaussian distribution, the largest is 20-30% greater than the next. This is representative of the large-amplitude statistics for the number of horizon waves within one tangent-horizon pixel.

8. F.X. Kneizys, E.P. Shettle, L.W. Abreu, J.H. Chetwynd, G.P. Anderson, W.O. Gallery, J.E.A. Selby, S.A. Clough, "User's Guide to LOWTRAN 7," AFGL-TR-88-0177, Aug. 1988.

9. E. H. Takken, R. G. Priest, E. P. Shettle, and J. C. Kershenstein, "IR Horizon Phenomenology: Report on IRAMMP Field Test," Proceedings of the 1991 Meeting of the IRIS Specialty Group on Targets, Backgrounds, and Discrimination, January 1991, ERIM document 213400-78-X(I).

ACKNOWLEDGMENTS

This work was funded by the Office of Naval Research.

NRL thanks Douglas Crowder and his personnel from NSWC, White Oak, for their help with logistics and for providing meteorological data. We thank the personnel of Areté Associates and NCCOSC for providing meteorological data. We also thank Linda Padgett, John Blackwell, and their co-workers at Amber Engineering for preparing the sensor and data acquisition system ahead of schedule.

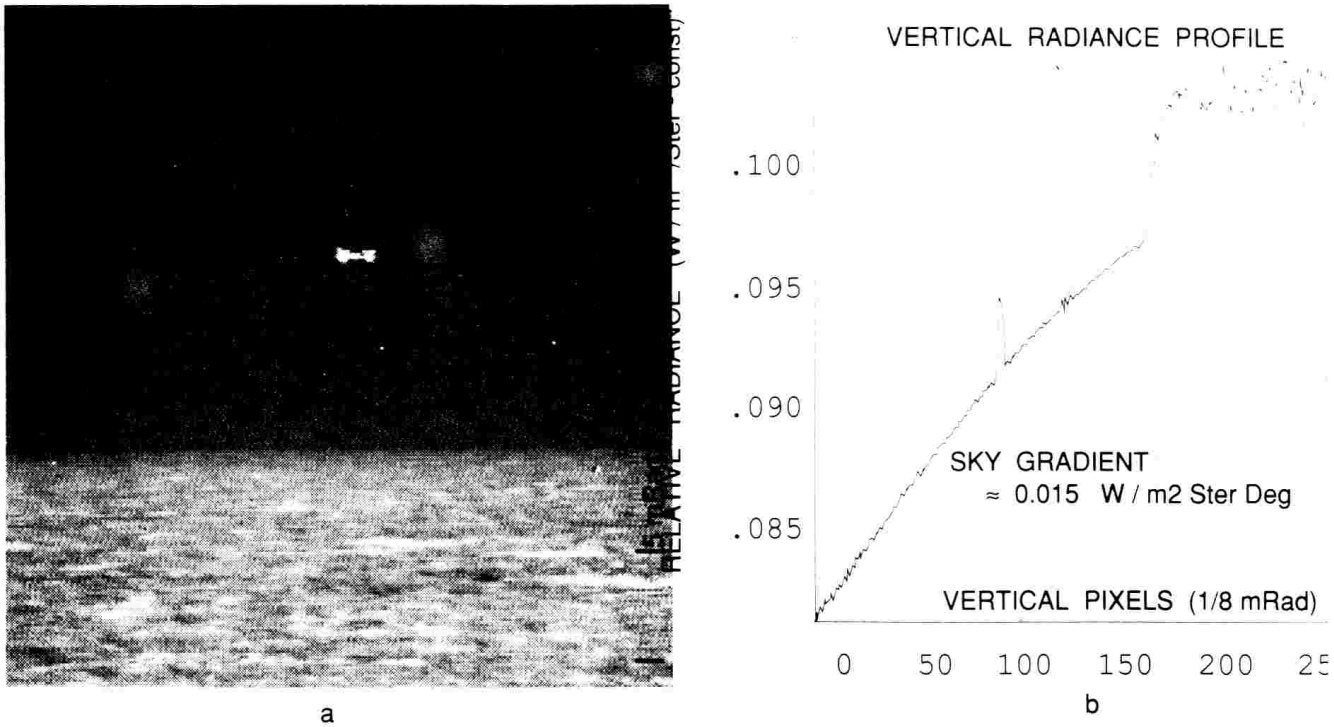

Fig. 1: NCCOSC aircraft (a) and row-averaged vertical radiance profile (b). The time is 4:42 pm with the sun low and far to the right and ASTD ≈ -2.6 °C but Gulf Stream passing the tower. Water speckle is due to wave-slope-induced variability in reflected sky radiation and water emissivity. The radiance rise at the horizon is smoothed by atmospheric attenuation and path emission and is positive because the air is cooler than the water. [Scene ThAC2]

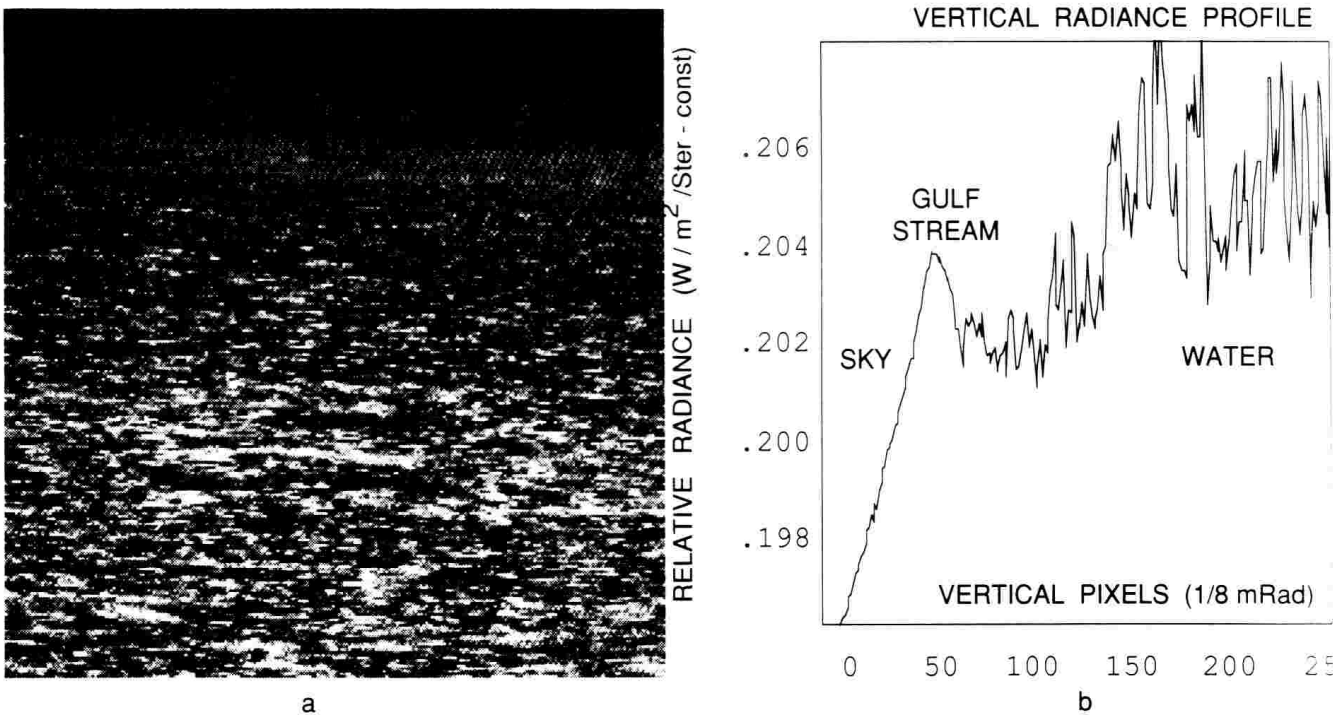

Fig. 2: Night radiance speckle (a) and row-averaged vertical radiance profile (b). The time is 9:33 pm looking east to the Gulf Stream with the moon directly overhead at 40° elevation and ASTD ≈ +1.0 °C at the tower. A view 30° to the right had nearly the same wave-surface IR speckle. The rise in the foreground speckle may be due to reflected radiance from a cloud. [SceneWMG1]

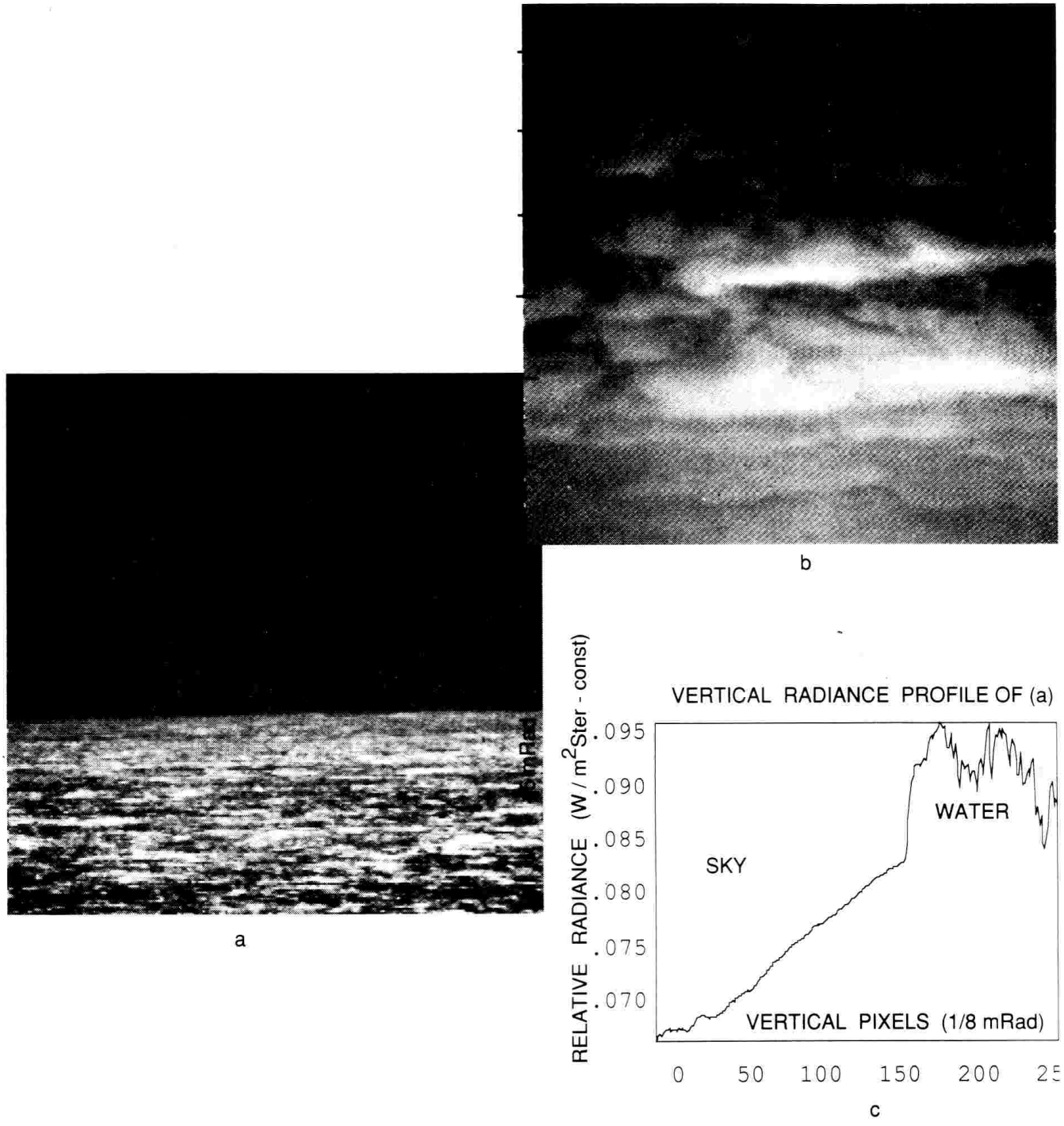

Fig.3: Bright night time IR surface speckle (a), warm bottom illuminated clouds at higher elevation (b) and the row-averaged vertical radiance profile (c). These IR images were taken the day after Fig. 2, though at the same time, 9:33 pm. The look direction is the same for both, to the south with the Gulf Stream and the moon far to the left. Sea state is modest and ASTD ≈ -3.2 °C at the tower. The displays are displaced in order to identify the matching cloud patterns, and the grey scales have been shifted for printing contrast clarity. [Scenes FrNR1 and FrNR2]

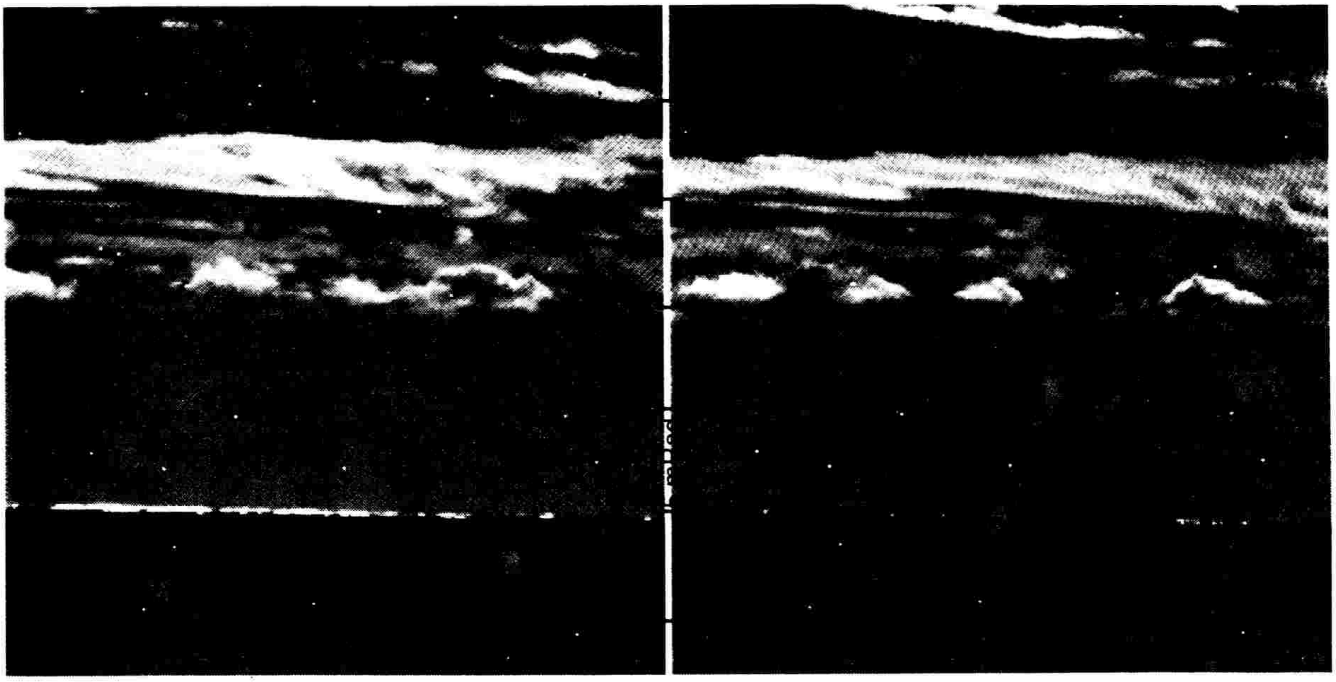

a b

Fig.4: Horizon glint with shadowed foreground. There is strong ray upbending due to an ASTD on the order of -7 to -10 °C. In these views looking south the noon-time winter sun is directly above the scenes at 30° elevation. In (a) there are often two of the 1/8 mRad pixels filled with solar glint at the horizon. The radiance transition from sky to glint to shadowed water is 0.20, 0.27, 0.16 W/m2Ster. In (b) two minutes different in the same view direction the shadowing had changed so that there are only single glint pixels, sometimes with a raised water pixel above. Cloud structure is 1.3x10-14 W/cm2 within or below the larger cloud band at 15 mRad and 2.2x10-14 W/cm2 over a larger retion. [Scenes FrGH2 and FrGH1]

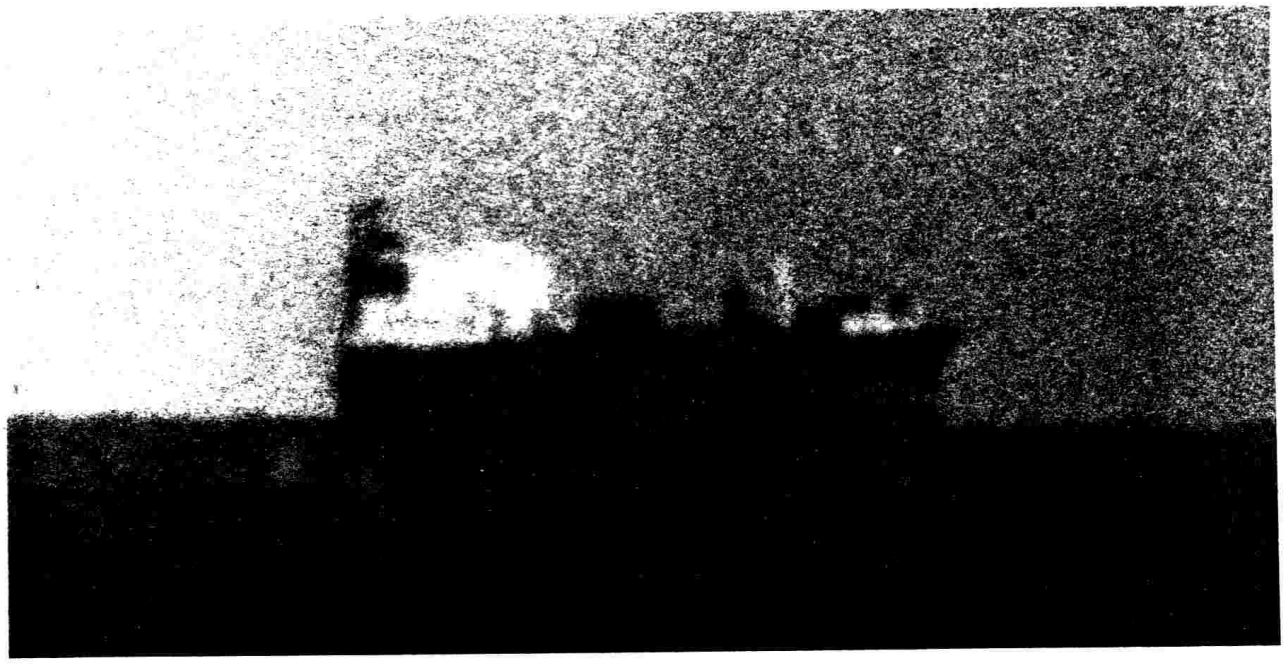

Fig. 5: Visible photograph of tanker just past the horizon toward Gulf Stream when an ASTD ≈ -4.5 to -5.0 °C at the tower. The vertical lines of the ship bow and mirage bow are straight right down to the water although the horizon line is quite wavy due to turbulence and/or the peak wave effect. The union of the true and mirage images occurs at ≈ 250 μRad above the geometric horizon. This is the apparent elevation angle at which a distant point target can first be seen and is therefore above the worst low-path turbulence.

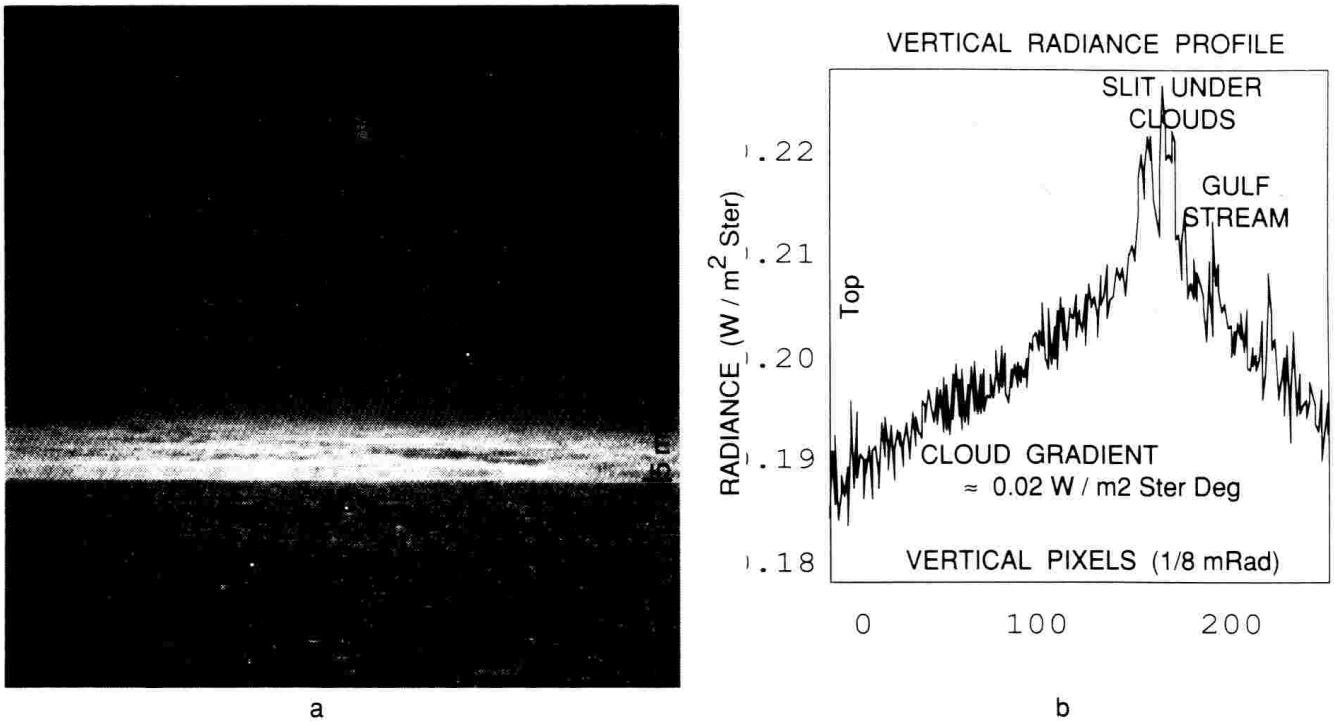

Fig. 6: Low-elevation cloud structure (a) and vertical radiance profile (b). The view to the east is over the Gulf Stream with ASTD ≈ -8 °C at the tower. A 2-3 mRad slit under dense clouds is being strongly back lit just after sun rise at 6:09 am. The structure in an ≈ 2 mRad square in this region is 6.5x10-15 W/cm2. [Scene ThSR2]

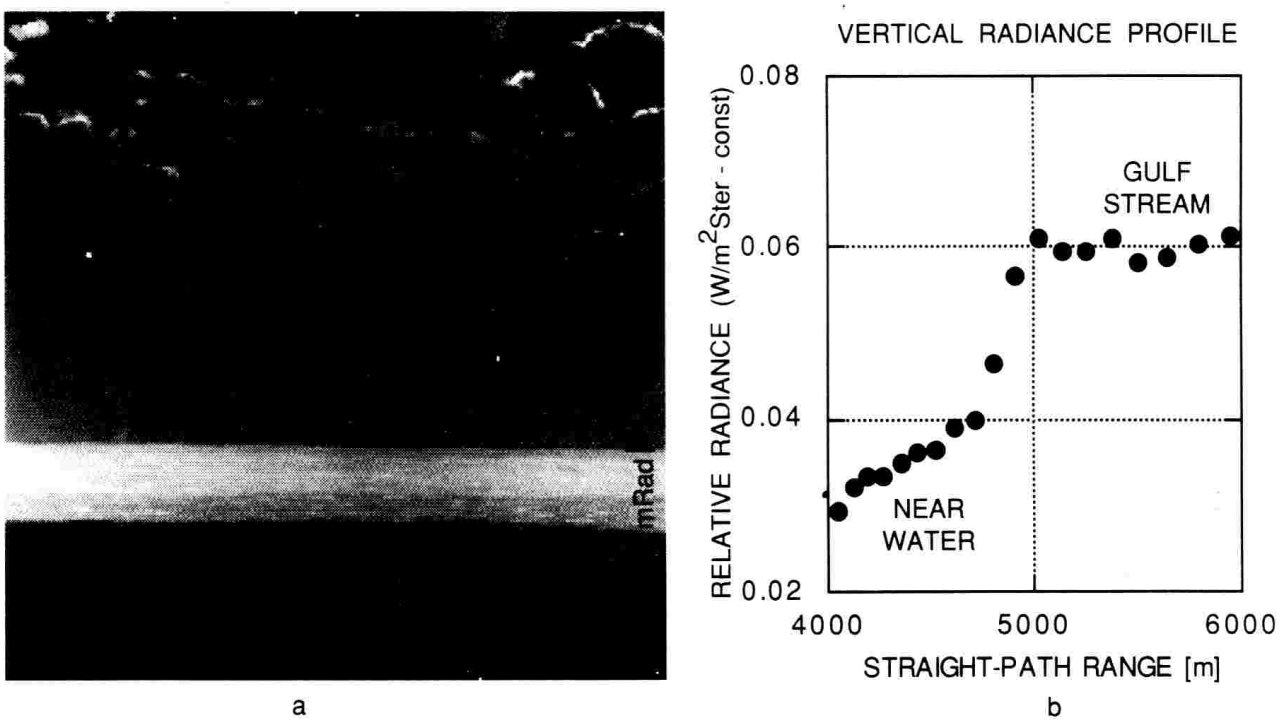

Fig. 7: Gulf Stream (a) and vertical radiance profile (b). The view is 120° SSE at 6:09 am just after sun rise and ASTD ≈ -4.7 °C at the tower. In (b) pixel position has been converted to range from the sensor so that the vertical-column radiance profile can be given as a function of position across the water surface. It shows a radiance discontunity across the Gulf Stream boundary of 0.020 W/m2Ster. The calculated value is 0.028 W/m2Ster. [Scene WSR2]

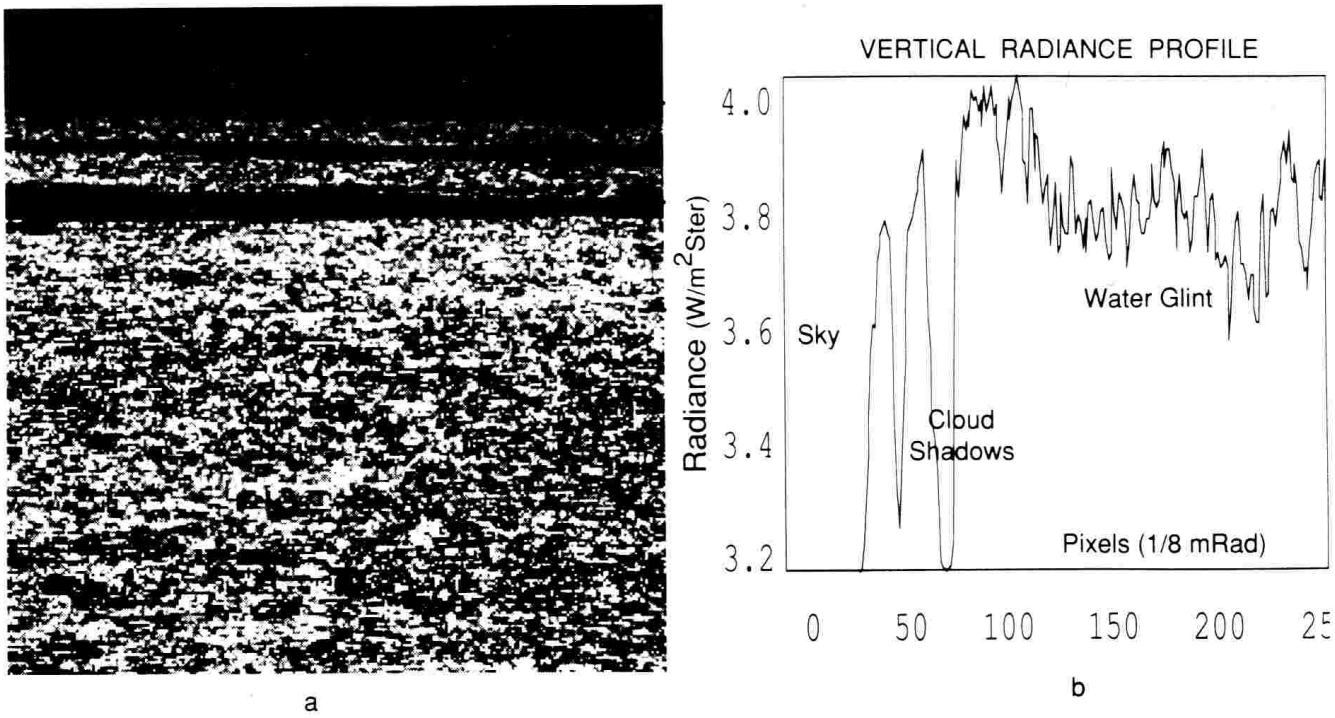

Fig. 8: Solar glint with shadows (a) and column-averaged vertical radiance profile (b). The time is 12:35 pm looking south with the sun over the scene at 36° elevation. The radiance step across the shadow-glint interface on the water surface is observed to be 0.75 W/m2Ster and the calculated value is 0.96 W/m2Ster. [Scene WSG1]

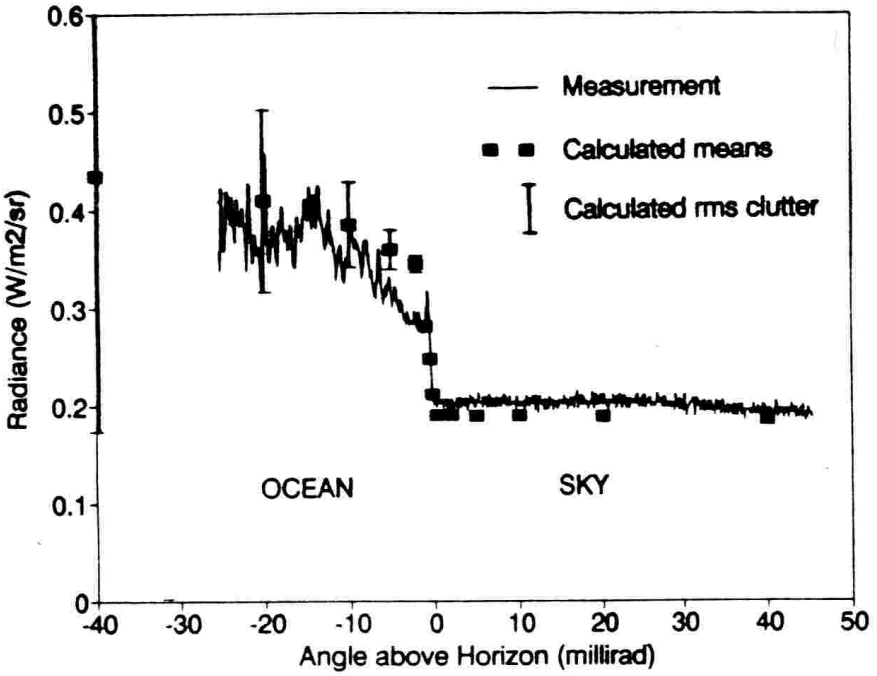

Figure 9. Vertical scan of horizon radiance profile from the Key90 data of the IRAMMP sensor. The data are row averages of 120 pixels. The filled squares represent the mean radiance predictions; the "error" bars represent the clutter. The waveband is 3.89 to 4.06 μm. The ASTD is -0.5C. [KEY90 Scene 0020-014]

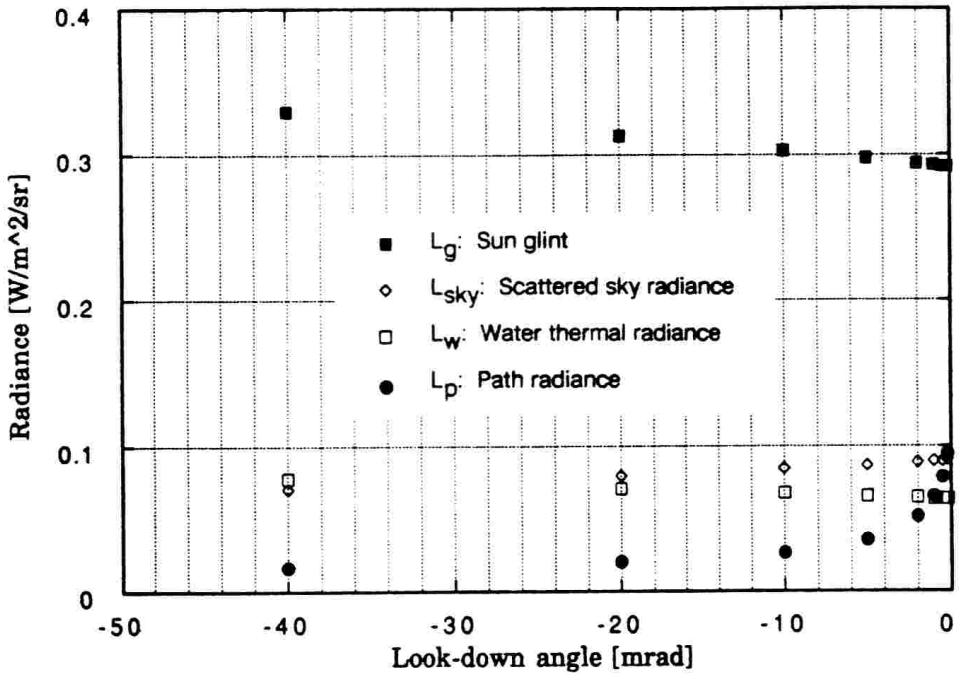

Figure 10. Calculation of components of ocean surface radiance for the Key90 data. The reflected sky radiance includes contributions from both sky radiance and scattered sunlight. Glint, reflected sky and water radiance values are given at the water surface before path attenuation.

APPENDIX : THEORY OF SURFACE RADIANCE WITH GLINT

A recent analysis has computed the radiance discontinuity associated with the ocean/sky interface at the horizon.[A1] The model presented in this report extends this analysis to the estimation of the observed radiance and radiance clutter in a range of look angles of ±40 mrad about the horizon.

The analysis of the measured radiance proceeds from the diagram presented in Figure A1. An ocean surface element, or wave facet, is shown in the x-z plane at an elevation z(**r**) where **r** is a location vector in the x-y plane. The elevation is measured relative to mean sea level. The surface element is tilted at an angle Θ having an x component in slope of $m_x = \tan(\Theta)$. A look-ray, emanating from a radiometer situated to the left of the diagram at a height h and making a negative angle ϵ with the horizontal, strikes the surface element. This ray is specularly reflected into a polar angle ϕ. The polar angle and surface element tilt angle are related by:

$$\phi(m_x,\epsilon) = (\pi/2) - 2\Theta(m_x) + \epsilon \qquad (1)$$

and are determined by the tilt slope m_x and look-down angle ϵ. Hence, downwelling radiance having a polar angle ϕ will be received by the radiometer. Also shown in Figure A1 is the sun positioned in the x-z plane at the solar zenith (i.e. polar) angle ϕ_s and exhibiting an angular width of $\Delta\phi_s$. The reflectivity $R(m_x,\epsilon)$ of the ocean surface element is determined by the Fresnel equations for unpolarized (i.e. natural) light. It is a function of the optical bandwidth averaged complex refractive index for water, the wave facet tilt slope and look-down angle. The complex refractive index is $n+i\kappa$ where n and κ are the real and imaginary components, respectively. The radiation received by the detector consists of five contributions: (i) the atmospheric path radiance emanating from the air column between the detector and the ocean surface, (ii) the thermal radiance emanating from the ocean surface element, (iii) the reflected downwelling sky radiance corresponding to the path from the ocean surface to space, (iv) the specularly reflected solar radiation or solar glint and (v) sunlight that is primarily forward scattered by aerosols present in the atmosphere and subsequently reflected by the ocean surface. Hence the total radiance (in $W/m^2/sr$) may be written as:

$$L(m_x,m_y,\epsilon) = L_p(\epsilon) + \tau(\epsilon)\, L_o(m_x,\epsilon) + \tau_s\, \tau(\epsilon)\, L_s(m_x,m_y,\epsilon) \qquad (2)$$

where it is understood that all radiances are band-limited by the detector filter. The atmospheric path radiance is $L_p(\epsilon) = [1-\tau(\epsilon)]\, L_a(T_a)$ where $\tau(\epsilon)$ is the transmission for an air column whose length is determined by the detector height and the look-down angle. $L_a(T_a)$ is the black body radiance corresponding to the air temperature T_a. The radiance $L_o(m_x,\epsilon)$ consists of three contributions:

$$L_o(m_x,\epsilon) = [1 - R(m_x,\epsilon)]\, L_w(T_w) + R(m_x,\epsilon)\, L_{sky} + R(m_x,\epsilon)\, L_{scat} \qquad (3)$$

where $L_w(T_w)$ is the blackbody radiance at the water temperature T_w, L_{sky} is the downwelling sky radiance and L_{scat} is the scattered sunlight. Note that the emissivity for the path radiance is $[1-\tau(\epsilon)]$ and that for the ocean surface is $[1-R(m_x,\epsilon)]$. The solar radiance, for small tilt slopes, is

approximated by:

$$L(m_x,m_y,\epsilon) = \begin{cases} L_s(T_s) & \text{where } m_c(\epsilon) - \Delta\phi_s/4 < m_x < m_c(\epsilon) + \Delta\phi_s/4 \\ & \quad \text{and } -\Delta\phi_s/2 < m_y < \Delta\phi_s/2 \\ 0 & \text{otherwise} \end{cases} \tag{4}$$

where $L_s(T_s)$ is the blackbody radiance of the sun at a solar temperature T_s and τ_s is the transmission from the sun to the ocean surface. The sun is specularly reflected into the detector for an m_x tilt slope range $\Delta\phi_s/2$ about a critical slope $m_c(\epsilon)$, given by

$$m_c(\epsilon) = \tan [\pi/4 - \phi_s/2 + \epsilon/2] \tag{5}$$

and an orthogonal tilt slope range in m_y of $\Delta\phi_s$ about zero.

The slopes m_x and m_y of the wave facets fluctuate with the water wave motion. These fluctuations may be described by a Gaussian probability density function (pdf):[A2]

$$p(m_x,m_y) = p_x(m_x)\, p_y(m_y) \tag{6}$$

where it is assumed that m_x and m_y are uncorrelated. The pdf for m_x is given by:

$$p_x(m_x) = (\pi/2)^{-1/2}\, \sigma_x^{-1} \exp(-m_x^2/2\sigma_x^2) \tag{7}$$

where σ_x^2 is the corresponding wave slope variance. This pdf is normalized for positive slopes since negative slopes are blocked from view. Note that this pdf has a mean tilt slope in the x direction of $\mu = \sigma_x \sqrt{(2/\pi)}$. The pdf for m_y has zero mean and is given by:

$$p_y(m_y) = (2\pi)^{-1/2}\, \sigma_y^{-1} \exp(-m_y^2/2\sigma_y^2) \tag{8}$$

where σ_y^2 is the corresponding slope variance. This pdf is normalized over all slope values. The principal quantities of interest are the surface element mean radiance $\langle L(\epsilon)\rangle$ and the root-mean-square (rms) radiance $L_{rms}(\epsilon)$. These are determined by the following integrals:

$$\langle L(\epsilon)\rangle = \int_{-\infty}^{\infty} dm_y \int_{0}^{\infty} dm_x\, p(m_x,m_y)\, L(m_x,m_y,\epsilon) \tag{9a}$$

$$L_{rms}^2(\epsilon) = \int_{-\infty}^{\infty} dm_y \int_{0}^{\infty} dm_x\; p(m_x,m_y)\, \{L^2(m_x,m_y,\epsilon) - \langle L(\epsilon)\rangle^2\} \tag{9b}$$

Evaluation of these integrals requires the wave slope variances σ_x^2 and σ_y^2. These quantities may be obtained from a Fourier description of the ocean surface.

Atmospheric winds generate ocean waves due to the work done by the wind on the roughened water surface. The wave height $z(\mathbf{r},t)$ at location $\mathbf{r}$ and time t may be represented by a superposition of plane waves:[A2]

$$z(\mathbf{r}, t) = \sum_{k} A_{\mathbf{k}} \exp[i(\mathbf{k} \bullet \mathbf{r} - \omega_{\mathbf{k}} t + \Psi_{\mathbf{k}})] \tag{10}$$

where $A_{\mathbf{k}}$ is the amplitude of the wave having a wave vector $\mathbf{k}$, angular frequency $\omega_{\mathbf{k}}$ and random phase $\Psi_{\mathbf{k}}$. The wave frequencies obey the dispersion relation:

$$\omega_{\mathbf{k}}^2 = g\,k\,[1 + \alpha k^2] \tag{11}$$

where g is the gravitational acceleration and $\alpha = T/\rho$ is the ratio of the water surface tension T and water density ρ. This dispersion relation describes gravity waves in the limit of small wave vectors and capillary waves for large wave vectors. The random phase $\Psi_{\mathbf{k}}$ reflects the random nature of the wind-generated Fourier components. The spectral composition of these water waves may be described by the wave height power spectral density (PSD) given by the Fourier transform of the wave height spatial correlation function:

$$S(\mathbf{k}) = (2\pi)^{-2} \int d\xi \, \langle z^*(\mathbf{r}) \bullet z(\mathbf{r}+\xi) \rangle_{\mathbf{r}} \exp(i\mathbf{k} \bullet \xi) \tag{12}$$

where ξ is a surface displacement vector and $\langle \ldots \rangle_{\mathbf{r}}$ denotes a spatial average over the ocean surface. This PSD has been extensively studied by the radar community. A recently refined expression developed by Donelan and Pierson[A3] is utilized in this analysis. The peak in the PSD appears at:

$$k_s = g / (1.2\,u_{10})^2 \tag{13}$$

where u_{10} is the wind speed measured at 10 m above the mean ocean surface. The large scale surface height variations are assumed to be dominated by a sinusoid with wave vector k_s and amplitude $A_s = \sqrt{2}\, z_{rms}$ where the rms wave height is:

$$z_{rms}^2 = \int d\mathbf{k}\, S(\mathbf{k}) \tag{14}$$

A numerical integration of this equation yields a square law dependence on wind speed for the rms wave height: $z_{rms} = 7.364 \times 10^{-3}\, u_{10}^2$. This dominant wave, or swell wave, is indicated in Figure A2. The exposure of a wave crest to the radiometer is limited by the shadowing of the preceding wave crest. The spatial extent x_o of the exposed wave crest is determined by the solution to the following equation:

$$\cos(k_s x) - \epsilon(\lambda_s - x)/A_s = 1 \tag{15}$$

where the swell wavelength $\lambda_s = 2\pi/k_s$. Note that the exposed wave crest dimension increases below the horizon as the radiometer peers into the trough of the swell wave.

Fluctuations in the facet slopes are characterized by the wave slope variances. The

downwind wave slope variance is given by the following integral:

$$\sigma_x^2 = \int_{-\pi}^{\pi} d\varphi \cos^2\varphi \int_0^{k_c} dk\ k^3\ S(k,\varphi) \qquad (16)$$

where viscous damping imposes a high frequency cutoff wave vector $k_c(u_{10}, T_w)$. The corresponding expression for the crosswind wave slope variance is:

$$\sigma_y^2 = \int_{-\pi}^{\pi} d\varphi \sin^2\varphi \int_0^{k_c} dk\ k^3\ S(k,\varphi) \qquad (17)$$

The wave slope variances σ_x^2 and σ_y^2 observed at a look angle χ relative to the downwind direction is obtained by the following coordinate rotation:

$$\sigma_{x'}^2 = \sigma_x^2 \cos^2\chi + \sigma_y^2 \sin^2\chi \qquad (18a)$$

$$\sigma_{y'}^2 = \sigma_x^2 \sin^2\chi + \sigma_y^2 \cos^2\chi. \qquad (18b)$$

Hence, the mean wave slope μ and the wave slope variances $\sigma_{x'}^2$ and $\sigma_{y'}^2$ are functions of the wind speed, look angle relative to the wind direction and the water temperature. These quantities may be utilized together with Eqs. (9a) and (9b) to compute the mean and rms wave facet radiances.

The radiometer measures a large number of ocean surface facets. The average radiance for N facets is equal to that calculated for a single facet. However, the rms radiance, or clutter, will be reduced by $\sqrt{N}$. The number of facets measured by a row of detector elements in the focal plane array may be computed by first estimating the size of a single facet. This may be accomplished by considering the normalized wave slope spatial correlation function:

$$\gamma_m(\xi) = \frac{\langle \nabla z^*(\mathbf{r}) \cdot \nabla z(\mathbf{r}+\xi) \rangle}{\langle\ |\ \nabla z(\mathbf{r})\ |^2 \rangle} \qquad (19)$$

which may be evaluated with the aid of the wave height PSD. The correlation length ξ_c is defined by $|\ \gamma_m(\xi_c)\ | = 0.5$ and is estimated to be 0.05 m. The ocean surface facet area is taken to be ξ_c^2. The exposed wave crest area is given by $\Delta\Phi\ z_R(\epsilon)\ x_o(\epsilon)$ where $\Delta\Phi$ is the sensor horizontal field-of-view and $z_R(\epsilon)$ is the range from the sensor to the ocean surface. The field of view is given by: $\Delta\Phi = M\ \phi_d$ where M is the number of individual detectors in a row of the focal plane array and ϕ_d is the detector field of view. In general, a single detector element will see many wave crests. The number of wave crests is approximately $k_s \Delta s(\epsilon)/2\pi$ where $\Delta s(\epsilon)$ is the single detector (or pixel) footprint on the ocean surface. The total number of facets measured is:

$$N(\epsilon) = \frac{\Delta\Phi \, z_R(\epsilon) \, x_o(\epsilon) \, k_s \, \Delta s(\epsilon)}{2\pi \, \xi_c^{\,2}} \tag{20}$$

Therefore, the clutter radiance is given by:

$$\Delta L_c(\epsilon) = L_{rms}(\epsilon) \, / \, \sqrt{N(\epsilon)} \tag{21}$$

Hence, this analysis supplies the mean radiance and clutter radiance measured by the radiometer as a function of look-down angle, meteorological conditions and sea state.

TABLE A1

Parameter Values used in the Key90 Data Analysis

$h = 31$ m	$k_c = 551\ m^{-1}$
$\phi_s = 0.94$ rad	$u_{10} = 4.0$ m/s
$\Delta\phi_s = 9.3$ mrad	$\sigma_x = 0.181$
$n = 1.38$	$\sigma_y = 0.163$
$\kappa = 0.015$	$\mu = 0.15$
$T_w = 30$ C	$\tau_s = 0.66$
$T_a = 29$ C	$\xi_c = 0.05$ m
$T_s = 5600$ K	$\phi_d = 0.25$ mrad
$L_w = 0.133\ W/m^2/sr$	$m_c = 0.3$
$L_a = 0.127\ W/m^2/sr$	$M = 120$
$L_s = 2.25 \times 10^4\ W/m^2/sr$	$R(\mu,\epsilon) = 0.44$

REFERENCES

A1. R.G. Priest, E.P. Shettle, and E.H. Takken, "High Resolution Imagery of the Sea Horizon: Data and Modeling," Proceedings, 1992 Meeting of the IRIS Specialty Group on Targets, Backgrounds, and Discrimination, January 1992, ERIM document 213400-128-X(I).

A2. M.A. Srokosz, "Wave Statistics," in *Surface Waves and Fluxes*, Volume I - Current Theory, ch. 9, ed. G. L. Geernaert and W. L. Plant (Kluwer Academic Publishers, Boston), 1990.

A3. M. A. Donelan and W. J. Pierson, Jr., "Radar Scattering and Equilibrium Ranges in Wind-Generated Waves with Application to Scatterometry," J. Geophys. Res. 92 (C5), 4971-5028 (1987).

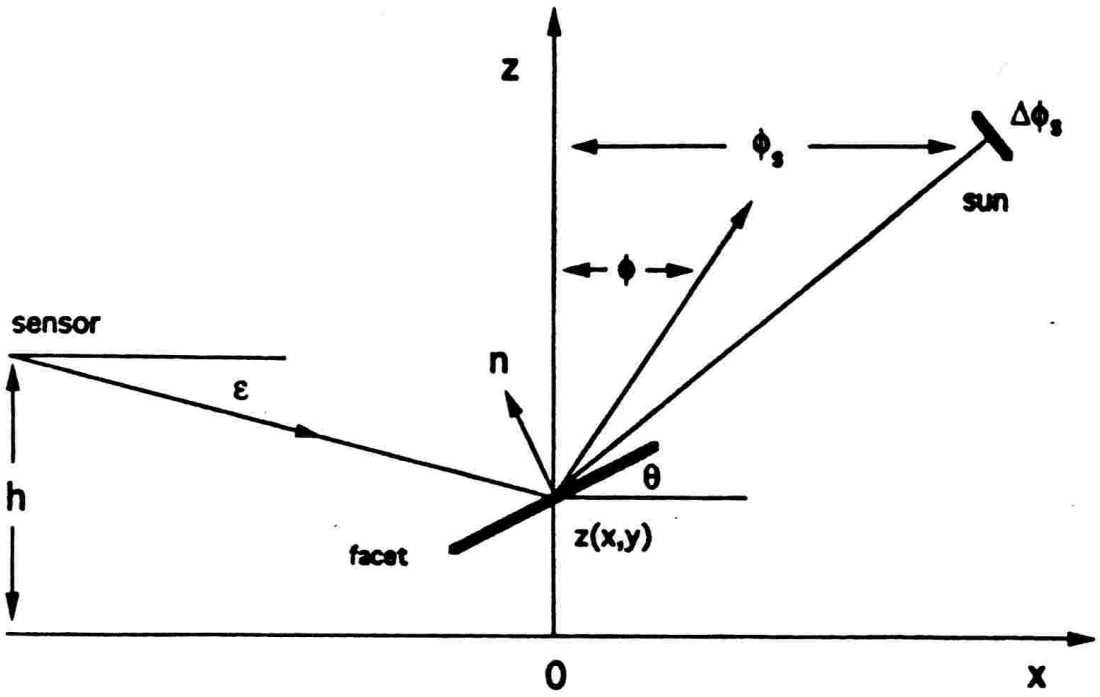

Figure A1. Angles involved in the calculation of reflection from an element (facet) of ocean surface. Definition of symbols is given in the text.

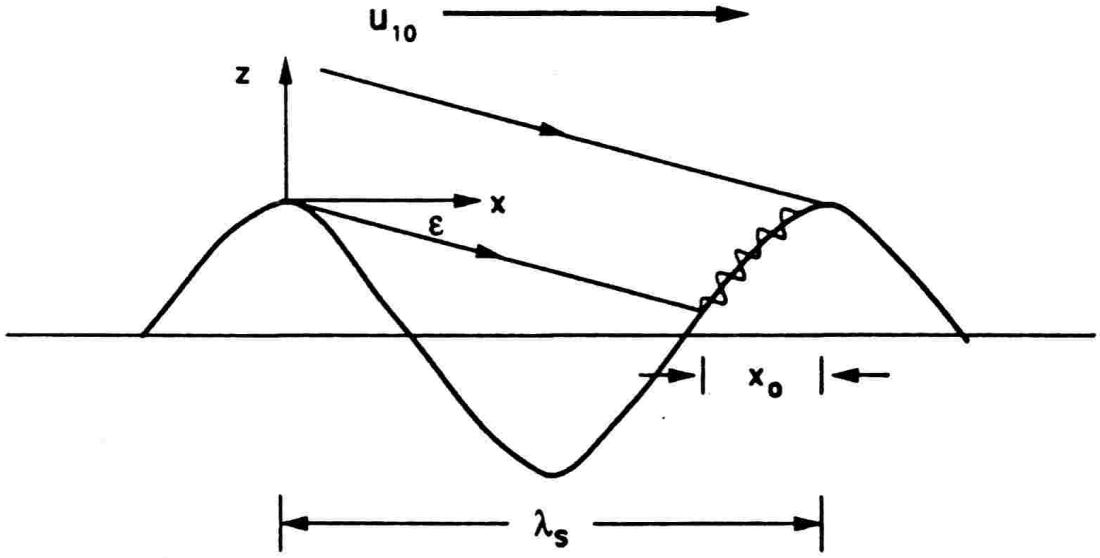

Figure A2. Geometry of reflection from ocean waves. A portion of the wave crest on the right is unobscured by the wave crest on the left, and contains many surface elements. Definition of symbols is given in the text.